Black Sea Journal of Engineering and Science
doi: 10.34248/bsengineering.1962591

Open Access Journal
e-ISSN: 2619 – 8991

Research Article
Volume 9 - Issue 4: 2094-2107 / July 2026

EFFECT OF STACKING SEQUENCE ON THE LOW-VELOCITY IMPACT BEHAVIOUR OF T300/5208 CARBON/EPOXY LAMINATES: AN INTRALAMINAR HASHIN-CDM BASED NUMERICAL STUDY OF EIGHT CONFIGURATIONS

Onur GÖK[1]*

[1]*Necmettin Erbakan University, Seydişehir Vocational School, Department of Machine and Metal Technologies, 42370, Konya, Türkiye*

Abstract: Carbon fiber reinforced polymer (CFRP) laminates are widely preferred in aerospace and transportation structures owing to their high specific strength and stiffness; however, they exhibit a pronounced sensitivity to out-of-plane low-velocity impact (LVI) loads. In this study, the effect of stacking sequence on the LVI response of T300/5208 CFRP laminates was investigated numerically. Eight stacking configurations (L1–L8), all 125 × 75 mm in size, 5 mm thick and consisting of 40 plies, were defined; unidirectional, cross-ply, angle-ply, quasi-isotropic, multidirectional, hybrid and blocked quasi-isotropic architectures were compared at a single controlled energy level. A hemispherical impactor with a mass of 5.5 kg was applied at an initial velocity of 2.468 m/s and an energy of 16.75 J. Numerical solutions were performed in Abaqus/Explicit using SC8R continuum shell elements together with the Hashin initiation criterion and an energy-based continuum damage mechanics (Hashin-CDM) framework; interlaminar separation was deliberately excluded within an intralaminar-only model. The geometry and post-processing were established on the basis of ASTM D7136. The results showed that the stacking sequence produced differences of about 53% in peak contact force, 38% in maximum displacement and 40% in permanently absorbed energy. The highest contact force and the smallest displacement were obtained for the cross-ply L3 (8964 N; 3.507 mm), whereas the lowest force and the largest displacement occurred for the unidirectional L2 (5863 N; 4.836 mm). In terms of permanent energy absorption, the angle-ply L4 reached the highest value (12.081 J). In all configurations, the dominant damage indicator was matrix tension damage (DAMAGEMT), and the damage orientations were consistent with the fiber directions. The results demonstrate that, through an appropriate choice of stacking sequence, the stiffness–energy absorption balance of the laminate under impact can be controlled.

Keywords: Carbon fiber reinforced polymer, Low-velocity impact, Stacking sequence, Finite element analysis, Hashin damage model, Intralaminar damage

***Corresponding author:** Necmettin Erbakan University, Seydişehir Vocational School, Department of Machine and Metal Technologies, 42370, Konya, Türkiye
E mail: ogok@erbakan.edu.tr (O. GÖK)
Onur GÖK https://orcid.org/0000-0003-1160-1963

Received: June 02, 2026
Accepted: July 11, 2026
Published: July 15, 2026

Cite as: Gök, O. (2026). Effect of stacking sequence on the low-velocity impact behaviour of T300/5208 carbon/epoxy laminates: An intralaminar Hashin-CDM based numerical study of eight configurations. *Black Sea Journal of Engineering and Science*, 9(4), 2094-2107.

1. Introduction

1.1. The Low-Velocity Impact Problem in CFRP Structures

Carbon fiber reinforced polymer (CFRP) laminates, owing to their high specific strength, specific stiffness and superior fatigue resistance, have risen to the position of a primary load-bearing material in many engineering fields such as aerospace, automotive, railway systems and marine applications (Abrate, 1998; Davies and Olsson, 2004). The fact that the use of composites in the fuselage and wing structures of modern commercial aircraft has reached significant proportions by weight progressively reinforces the role of this material class in load-bearing structural design. Nevertheless, the heterogeneous and orthotropic character at the fiber-matrix interface renders CFRP structures markedly sensitive to out-of-plane loads, particularly to low-velocity impact (LVI) effects (Abrate, 1991). Events such as tool drops, hail strikes or the projection of particles on the runway during manufacturing, assembly and service processes, although they leave traces too small to be detected visually on the surface, can lead to widespread matrix cracks and interlaminar separation within the internal structure.

Low-velocity impact is defined as a loading regime that typically occurs at contact velocities in the 1–10 m/s range and triggers a quasi-static-like response over a duration that allows the stress waves to reflect repeatedly across the specimen thickness (Abrate, 1991; Olsson, 2000). The mass-based boundary criterion proposed by Olsson (2000) reveals that the transition from a wave-controlled response to a plate-controlled response is observed when the ratio of the impactor mass to the specimen mass exceeds a certain threshold.

The most critical aspect of this regime from an engineering standpoint is the formation of the “barely visible impact damage” (BVID) pattern that cannot be detected by standard inspection methods, damage that can lead to considerable losses in compression after impact (CAI) residual strength (Ghelli and Minak, 2011; Guo et al., 2022; Zhao et al., 2024).

1.2. Numerical Modelling and Damage Mechanisms

Numerically capturing the progressive damage response of CFRP laminates under impact requires the appropriate modelling of both the damage initiation criterion and the damage evolution law (Huang et al., 2023). The anisotropic strength criteria developed by Hashin (1980), Puck and Schürmann (2002) and Tsai and Wu (1971) make it possible to evaluate the four fundamental damage modes in the fiber-matrix plane (fiber tension, fiber compression, matrix tension, matrix compression) separately. Huang et al. (2023) compared the predictive accuracies of the Hashin and Puck criteria and reported that the choice of the damage evolution law (sudden / linear / exponential softening) is more decisive than the choice of the damage initiation criterion. The formulation proposed by Lapczyk and Hurtado (2007), which is based on the continuum damage mechanics (CDM) framework of Matzenmiller et al. (1995), constitutes the analytical basis of the built-in Hashin damage module of the Abaqus/Explicit software.

In the relevant literature, Rezasefat et al. (2021) investigated the response of CFRP plates under repeated LVI by combining it with a cohesive-element-based interface model, whereas Zhou et al. (2020) revealed the effect of repeated impact on damage accumulation in cross-ply laminates using a three-dimensional Hashin criterion. A subsequent study by the same research group (Zhou et al., 2022) showed that, with increasing laminate thickness, the dominant damage mode shifts from intralaminar damage towards interlaminar separation. Ait Mohammed and Tarfaoui (2022) evaluated the effects of different quadratic criteria on cylindrical glass/epoxy structures through a user-defined subroutine. For thermoplastic-matrix systems, Han et al. (2024) and Mohsin et al. (2021) achieved agreement between the progressive damage model and the experimental force–time responses.

During LVI, multiple damage modes may occur simultaneously in composite laminates: matrix tension/compression cracks, fiber breakage, fiber-matrix debonding and interlaminar separation (Han et al., 2024; Shang et al., 2025). The relative contributions of these modes show a strong dependence on impact energy, geometry, boundary conditions and stacking sequence. Vlach et al. (2022) measured the strain field on the carbon/epoxy surface after impact using the digital image correlation method and showed that the distribution around the damage zone is sensitive to the laminate architecture. Xiong et al. (2023) demonstrated for natural-fiber composites that the damage morphology changes with the energy level, while Shang et al. (2025) proposed the concept of crack dissipation energy to quantify the damage severity and revealed that the primary damage mode changes with the energy level.

1.3. The Effect of Stacking Architecture

The laminate stacking architecture is the primary design variable that determines the balance between impact stiffness and energy absorption capability (Guo et al., 2022). In a numerical study conducted on eight different stacking sequences for semicylindrical woven composite shells, Ferreira et al. (2024) revealed that an increase in the impact-bending stiffness raises the maximum contact force but lowers the maximum displacement, the contact duration and the dissipated energy. In another study by the same group (Ferreira et al., 2023a), the numerical simulation of a semicylindrical woven shell was carried out and the role of ply positions in energy dissipation was emphasized. Albayrak et al. (2023), on the other hand, reported that, in rubber-interlayered curved sandwich composites, positioning the interlayer at the mid-plane considerably improves energy absorption. Guo et al. (2022) examined a subset of stacking parameters in a parametric LVI and CAI study, while Li et al. (2024) evaluated the effect of different hybridization strategies in hybrid woven carbon/aramid laminates.

For curved geometries, Seifoori et al. (2021) determined the effect of the radius of curvature on the mid-point deflection and the damage area under impact in CFRP and GFRP curved laminates. The LVI behaviour of curved composite panels used in air vehicles was investigated experimentally by Dağ et al. (2024) in terms of different stiffener elements, and the decisive role of the stiffener type on the contact force and damage propagation was demonstrated. The low-velocity impact behaviour of curved CFRP panels has also been investigated numerically in terms of curvature and stacking effects (Gök, 2026). For unidirectional prepreg systems, Hongkarnjanakul et al. (2013) showed that LVI modelling including fiber breakage for different stacking sequences was validated against experimental data. For more complex structures, Zhang et al. (2018) proposed a full-process numerical approach for stitched composites, while Rezasefat et al. (2023) addressed the effect of pre-existing impact damage on the subsequent LVI response, and Mutsuddy et al. (2025) addressed the repeated impact behaviour of hybrid woven laminates.

1.4. Literature Gap and the Original Contribution of This Study

Gómez-del Río et al. (2005) investigated the effect of stacking sequence on impact damage in CFRP laminates at low temperature; this study and those summarized above show that many variables affecting the LVI response have been addressed for different geometries, material systems and energy levels. Nevertheless, three open gaps exist in the literature. The majority of studies that systematically examine the stacking architecture rely either on curved/cylindrical geometries (Seifoori et al., 2021; Albayrak et al., 2023; Ferreira et al., 2024) or on a small number of configurations, and studies that directly compare eight different stacking architectures at a single controlled impact energy level on flat CFRP panels are rare. Most of these studies were moreover conducted at arbitrary or experimental energy levels, and systematically designed controlled comparisons based on the thickness-normalized protocol of ASTM D7136 (ASTM International, 2012) have remained scarce. The direct comparison of a dispersed quasi-isotropic stacking with a blocked quasi-isotropic stacking (ply-blocking) has, on the other hand, been made only indirectly in the literature.

This study presents four fundamental contributions: (i) the modelling of eight different stacking configurations (L1–L8), 5 mm thick and 125 × 75 mm in size, based on the T300/5208 prepreg system, within a unified numerical framework using SC8R continuum shell elements in the Abaqus/Explicit environment; (ii) the establishment of a single-variable controlled comparison in which the ASTM D7136 specimen geometry and post-processing protocol are taken as the basis but the impact energy is set to C_e = 3.35 J/mm (16.75 J) so as to target the medium-low regime; (iii) the derivation of a configuration-dependent performance map in terms of maximum contact force, contact duration, maximum displacement, absorbed energy and the dominant intralaminar damage indicator (DAMAGEMT); (iv) the quantification of the ply-blocking effect through the direct comparison of the dispersed $[0/45/\text{-}45/90]_{5s}$ and blocked $[0_5/45_5/\text{-}45_5/90_5]_s$ quasi-isotropic stackings within the same numerical scope.

The scope of the study was deliberately limited to intralaminar damage mechanisms, and a cohesive interface model for interlaminar separation (delamination) was not included in this study within the intralaminar-only model framework; the effect of this methodological choice on the results is evaluated in the discussion section.

2. Materials and Methods

2.1. Material System

The material system used in this study is the unidirectional prepreg system consisting of T300 carbon fiber and 5208 epoxy resin, which is widely used as a reference in aerospace applications. The orthotropic elastic properties and strength parameters at the lamina level were defined on the basis of the values reported by Tsai and Hahn (1980) and are summarized in Table 1.

Table 1. T300/5208 lamina properties

Parameter	Symbol	Value	Unit
Longitudinal modulus of elasticity	E_1	181000	MPa
Transverse modulus of elasticity	E_2	10300	MPa
Shear modulus (12, 13)	$G_{12} = G_{13}$	7170	MPa
Shear modulus (23)	G_{23}	3678	MPa
Poisson's ratio (12)	ν_{12}	0.28	–
Poisson's ratio (23)	ν_{23}	0.40	–
Density	ρ	1.54×10^{-9}	ton/mm^3
Longitudinal tensile strength	X_t	1500	MPa
Longitudinal compressive strength	Xc	1500	MPa
Transverse tensile strength	Y_t	40	MPa
Transverse compressive strength	Yc	246	MPa
Longitudinal shear strength	SL	68	MPa
Transverse shear strength	S_t	68	MPa
Fiber tensile fracture energy	Gf_t	91.6	N/mm
Fiber compressive fracture energy	Gfc	79.9	N/mm
Matrix tensile fracture energy	G_{mt}	0.22	N/mm
Matrix compressive fracture energy	G_mc	1.10	N/mm

The density value was taken as 1.54×10^{-9} ton/mm^3, and the shear modulus G_{23} was calculated as 3678 MPa using the relation in equation 1 under the assumption of a transverse Poisson's ratio ν_{23} = 0.40. The symmetric fiber-failure assumption in which the tensile and compressive strengths in the fiber direction are taken to be equal (X_t = Xc = 1500 MPa) is consistent with the formulation of the Hashin initiation criterion (Hashin, 1980). The transverse shear strength was assumed to be equal to the longitudinal shear strength (S_t = SL = 68 MPa) since no separate experimental data were available (equation 1).

$$G_{23} = \frac{E_2}{2(1+\nu_{23})} \tag{1}$$

The fracture energies required for the intralaminar damage evolution were based on the values obtained by Pinho et al. (2006) from compact tension and compression tests: fiber tension Gf_t = 91.6 N/mm; fiber compression Gfc = 79.9 N/mm. The fracture energies in the matrix direction were taken from the values reported by Krueger (2005): matrix tension G_{mt} = 0.22 N/mm; matrix compression G_mc = 1.10 N/mm. Since for T300/5208 not all fracture energies could be obtained from the same experimental data set, they were taken from the closest literature systems, which is an accepted engineering approach. These energy parameters were provided directly as inputs to the linear-softening energy-based damage evolution law (Lapczyk and Hurtado, 2007).

2.2. Geometry and Stacking Configurations

The specimen geometry used in the numerical model was chosen as 125 × 75 × 5 mm in accordance with the dimensions defined in the ASTM D7136 (ASTM International, 2012) standard. The standard specifies a 40-ply $[45/0/-45/90]_{5s}$ quasi-isotropic stacking as the reference laminate for unidirectional prepregs with a nominal lamina thickness in the 0.10–0.13 mm range. In the present study, a nominal lamina thickness of 0.125 mm was assumed and the total number of plies was kept fixed at 40 for all configurations; thus the laminate thickness, density and consequently the dynamic response mass remained the same in all cases, and only the effect of the stacking architecture was isolated.

The eight stacking configurations examined are listed in Table 2. The configurations can be grouped by class as follows: unidirectional laminates (L1, L2), cross-ply laminate (L3), angle-ply laminate (L4), quasi-isotropic laminate (L5, the ASTM standard reference), multidirectional laminate (L6), hybrid stacking laminate (L7) and blocked quasi-isotropic laminate (L8). The 0° fiber direction was aligned along the panel length (the 125 mm direction). While L1–L6 and L8 are symmetric stackings, the hybrid L7 is the only non-symmetric configuration; therefore a limited extension-bending coupling may be expected in L7, but since identical boundary conditions and impact energy were applied to all configurations the relative comparison is preserved.

Table 2. The eight stacking configurations examined (0° aligned along the panel length; L5 is the rotated equivalent of the ASTM reference $[45/0/-45/90]_{5s}$)

Code	Stacking sequence	Class
L1	$[0]_{40}$	Unidirectional 0°
L2	$[90]_{40}$	Unidirectional 90°
L3	$[0/90]_{10s}$	Cross-ply
L4	$[+45/-45]_{10s}$	Angle-ply
L5	$[0/45/-45/90]_{5s}$	Quasi-isotropic (ASTM)
L6	$[0/30/60/90]_{5s}$	Multidirectional
L7	$[+30/-30/+60/-60/0/90/+45/-45]_{5}$	Hybrid
L8	$[0_5/45_5/-45_5/90_5]_s$	Blocked quasi-isotropic

2.3. Finite Element Model

The numerical simulations were performed in the Abaqus/Explicit environment. Explicit time integration was preferred because it was found more suitable than implicit methods, both in terms of computational cost and convergence behaviour related to damage evolution, for capturing the high-speed transient dynamic response of composite laminates under impact (Belytschko et al., 1984). The specimen was discretized with the SC8R continuum shell element type (eight-node, reduced integration). Continuum shell elements are widely used in LVI applications because they combine the simplicity of conventional shell elements with the ability to capture the stress distribution through the thickness in thick laminates (Zhou et al., 2020; Rezasefat et al., 2021). The in-plane element size was locally refined to 1 mm × 1 mm around the impact point and gradually coarsened towards the specimen edges. The total number of elements was kept fixed at 154196 for all configurations, and each lamina was represented by a single SC8R element through the thickness.

The impactor was modelled as a rigid body with a 16 mm diameter hemispherical tip in accordance with the geometry described in the ASTM D7136 (ASTM International, 2012) standard. The total impactor mass was 5.5 kg and was concentrated on a reference point; the 16 mm diameter hemispherical impactor is a configuration widely adopted in CFRP impact tests within a similar energy and thickness range (Cao et al., 2020). The interaction between the specimen and the impactor was defined using the general contact algorithm of Abaqus/Explicit, and the friction coefficient in the tangential direction was taken as μ = 0.3. The normal contact behaviour was defined by a hard contact pressure-overclosure relationship, and no viscous contact damping or artificial stabilization was applied. No mass scaling was employed in the explicit time integration, and solution stability was ensured solely by the stable time increment of Abaqus/Explicit.

2.4. Boundary Conditions and Impact Conditions

The boundary conditions were applied so as to represent the four-clamp support arrangement defined by ASTM D7136 (ASTM International, 2012). In the regions where the specimen is in contact with the clamps, all translational and rotational degrees of freedom were set to zero ($U_1 = U_2 = U_3 = 0$; $UR_1 = UR_2 = UR_3 = 0$), and for the impactor only translational freedom along the vertical axis was left. These boundary conditions are shown schematically in Figure 1. Although this node-based constraint does not fully represent the real clamp contact mechanics, the relative comparison is preserved since it is applied identically to all eight stackings.

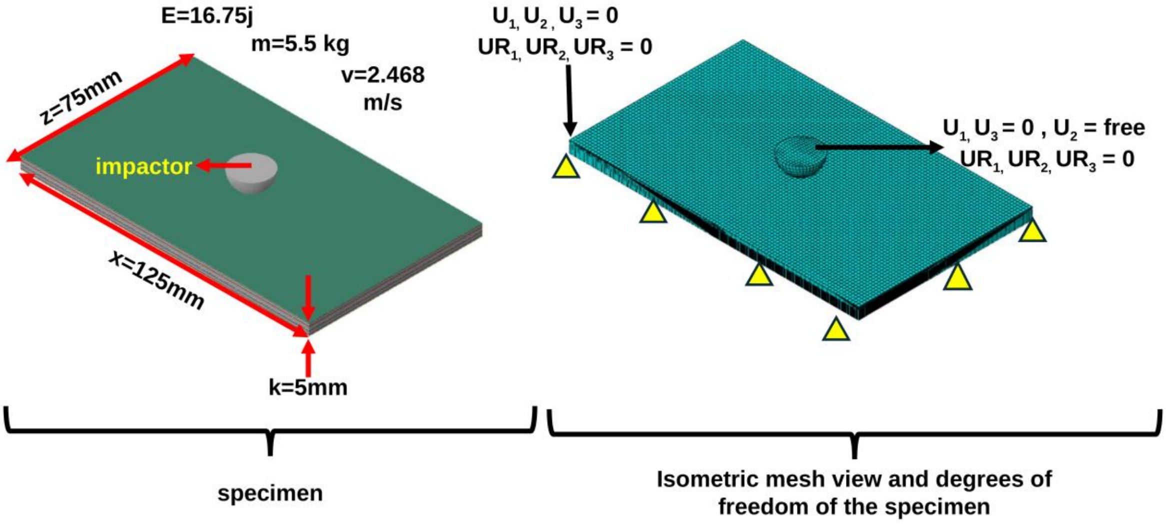

Figure 1. Specimen geometry, impact conditions, applied boundary conditions and the finite element mesh.

The impact energy was calculated on the basis of the thickness-normalized expression given by ASTM D7136 (ASTM International, 2012). In the present study, a value of C_e = 3.35 J/mm was adopted and the nominal impact energy was obtained as 16.75 J by means of equation 2 (h = 5 mm); this level corresponds to half of the reference value of C_e = 6.7 J/mm recommended by ASTM D7136 for unidirectional prepreg laminates and is consistent with previous studies (Zhou et al., 2022; Rezasefat et al., 2023) targeting the medium-low energy regime in which damage initiation and evolution are limited. This energy corresponds to the initial velocity v_i = 2.468 m/s obtained from the kinetic energy equation (equation 3) of the constant-mass (m = 5.5 kg) impactor. All eight configurations were subjected to the same 16.75 J energy and the same 2.468 m/s initial velocity, providing a single-variable controlled comparison. In equation 2, C_e denotes the thickness-normalized impact energy coefficient and h the laminate thickness; in equation 3, m denotes the impactor mass and E the impact energy.

$$E = C_e\, h \tag{2}$$

$$v_i = \sqrt{\frac{2E}{m}} \tag{3}$$

2.5. Intralaminar Damage Model (Intralaminar-Only Model)

For intralaminar damage initiation, the four-mode criterion proposed by Hashin (1980) was adopted: fiber tension ($\sigma_{11} \geq 0$), fiber compression ($\sigma_{11} < 0$), matrix tension ($\sigma_{22} \geq 0$) and matrix compression ($\sigma_{22} < 0$) (equations 4–7). The attainment of a value of 1 by any of these criteria at an integration point results in the initiation of the corresponding damage mode. After damage initiation, the damage evolution was represented by the linear-softening energy-based formulation developed by Lapczyk and Hurtado (2007), which is based on the continuum damage mechanics framework of Matzenmiller et al. (1995) (equations 8–10). The damage variables df_t, dfc, d_{mt} and d_mc vary between 0 (intact) and 1 (fully damaged), and the output definitions in Abaqus/Explicit were tracked as DAMAGEFT, DAMAGEFC, DAMAGEMT and DAMAGEMC, respectively. In the damage initiation criteria (equations 4–7), σ_{11} and σ_{22} denote the normal stresses in the fiber and transverse directions respectively, τ_{12} the in-plane shear stress; X_t, Xc, Y_t, Yc and S_L the corresponding strength values given in Table 1; and α the shear contribution coefficient in the fiber tension criterion (α = 1 in this study). In the equations defining the damage evolution (equations 8–10), C denotes the undamaged stiffness matrix, ε the strain, d_i the damage variable of the corresponding mode; δ_i^0 and δ_i^f the damage-initiation and full-damage equivalent displacements of the corresponding mode; σ_i^0 the initiation stress, G_i the fracture energy in Table 1 and Lc the characteristic element length.

$$\text{Fiber tension } (\sigma_{11} \geq 0) \left(\frac{\sigma_{11}}{X_t}\right)^2 + \alpha\left(\frac{\tau_{12}}{S_L}\right)^2 \geq 1 \tag{4}$$

$$\text{Fiber compression } (\sigma_{11} < 0) \left(\frac{\sigma_{11}}{X_c}\right)^2 \geq 1 \tag{5}$$

$$\text{Matrix tension } (\sigma_{22} \geq 0) \left(\frac{\sigma_{22}}{Y_t}\right)^2 + \left(\frac{\tau_{12}}{S_L}\right)^2 \geq 1 \tag{6}$$

$$\text{Matrix compression } (\sigma_{22} < 0) \left(\frac{\sigma_{22}}{2S_T}\right)^2 + \left[\left(\frac{Y_c}{2S_T}\right)^2 - 1\right]\frac{\sigma_{22}}{Y_c} + \left(\frac{\tau_{12}}{S_L}\right)^2 \geq 1 \tag{7}$$

$$\sigma = (1 - d_i)\, C\, \varepsilon \tag{8}$$

$$d_i = \frac{\delta_i^f\,(\delta_i - \delta_i^0)}{\delta_i\left(\delta_i^f - \delta_i^0\right)} \tag{9}$$

$$G_i = 1/2\ \sigma_i^0\, \delta_i^f\, L_c \tag{10}$$

Although the Puck criterion (Puck and Schürmann, 2002) or the Tsai-Wu criterion (Tsai and Wu, 1971) could be used as alternatives, the comparative study of Huang et al. (2023) showed that the Hashin and Puck criteria produce similar predictions in terms of the global response, but that the functional form of the damage evolution is more decisive on the results. Accordingly, the Hashin criterion and linear energy-based softening were preferred in the present study. The interlaminar separation (delamination) model was excluded from the scope of the study in accordance with the intralaminar-only model approach, and an analysis extended with the cohesive interface formulation (Camanho et al., 2003) was left to future work.

2.6. ASTM D7136-Based Post-Processing

Only the impactor-specimen contact force F(t) was obtained directly as the Abaqus/Explicit output; the impactor velocity v(t), the displacement δ(t) and the energy $E_a(t)$ absorbed by the specimen were derived through analytical integration on the basis of ASTM D7136 (ASTM International, 2012) (equations 11–13). The impactor velocity was computed from the integral of the force time history, and the displacement from one further integration of the velocity. The numerical integrations were performed with the trapezoidal rule using a step equal to the sampling time step (Δt = 0.03 ms). The maximum contact force F_{max}, the energy E_{max} absorbed at the instant corresponding to this force, and the permanent absorbed energy Ef_{inal} obtained at the end of the contact duration were extracted in accordance with their standard definitions. In equations 11-13, F(τ) denotes the time history of the contact force, g the gravitational acceleration, m the impactor mass, v_i the initial velocity, and τ and s the integration variables.

$$v(t) = v_i + g\,t - \frac{1}{m}\int_0^t F\,(\tau)\,d\tau \tag{11}$$

$$\delta(t) = v_i\,t + 1/2\,g\,t^2 - \frac{1}{m}\int_0^t \left[\int_0^s F\,(\tau)\,d\tau\right]ds \tag{12}$$

$$E_a(t) = 1/2\,m\left[v_i^2 - v(t)^2\right] + m\,g\,\delta(t) \tag{13}$$

2.7. Mesh Convergence and Numerical Controls

In order to evaluate the dependence on element size, a mesh convergence analysis was performed on the quasi-isotropic reference configuration (L5) by varying the in-plane element size around the impact point at values of 0.8 mm, 1.0 mm and 1.25 mm. The relative difference between the 0.8 mm and 1.0 mm sizes was calculated as 2.1% in terms of F_{max}, 1.8% in terms of δ_{max} and 3.4% in terms of Ef_{inal}; it was determined that the 1.0 mm element size exhibited a reasonable convergence and, considering the computational cost, was adopted for all subsequent analyses. In order to assess the numerical reliability, the fundamental energy components of Abaqus/Explicit were monitored, and the ratio of the artificial energies (ALLAE) to the internal energy (ALLIE) remained below 3% for all eight configurations (Belytschko et al., 1984). Mass scaling was not used. The good agreement of similar Abaqus/Explicit and Hashin-based LVI setups with experimental force–time responses was shown by Sun et al. (2018) for glass/epoxy laminates, which constitutes a reference supporting the reliability of the present model at the global response level. The bending-dominated transient response of the laminate under impact is qualitatively consistent with the bending stiffness distribution predicted by classical lamination plate theory (Reddy, 2003); the fact that the cross-ply L3, in which the 0°/90° pairs provide high bending stiffness along the panel length, yields the highest contact force supports the expectation of this framework.

3. Results

3.1. General Overview of the Impact Response Parameters

The Abaqus/Explicit simulations of the eight stacking configurations were post-processed on the basis of ASTM D7136 (ASTM International, 2012), and the obtained impact response parameters are given collectively in Table 3. In all configurations the maximum absorbed energy E_{max} remained in the 16.94–17.01 J range, just above the nominal impact energy (16.75 J); this narrow range shows that the controlled single-variable comparison was established consistently in terms of energy input. The maximum contact force F_{max}, the contact duration t_t, the maximum displacement δ_{max} and the permanent absorbed energy Ef_{inal}, on the other hand, showed a strong dependence on the configuration.

Table 3. ASTM D7136-based impact response parameters for the eight stacking configurations (m = 5.5 kg; v_i = 2.468 m/s; nominal E = 16.75 J)

Config.	F_{max} (N)	t_t (ms)	δ_{max} (mm)	E_{max} (J)	Ef_{inal} (J)
L1	7065	4.77	4.283	16.98	9.984
L2	5863	5.76	4.836	17.01	8.643
L3	8964	3.93	3.507	16.94	10.183
L4	7560	4.65	4.542	16.99	12.081
L5	8637	4.11	3.890	16.96	10.594
L6	8427	4.26	3.908	16.96	10.032
L7	8487	4.23	4.006	16.97	10.196
L8	8241	4.53	4.256	16.98	10.479
Mean	7906	4.53	4.16	16.97	10.28
Std. deviation	1027	0.57	0.42	0.02	0.94
CV (%)	13.0	12.6	10.0	0.1	9.2

In order to quantitatively evaluate the variability among the configurations, the mean, the standard deviation and the coefficient of variation (CV) were calculated over the eight values for each parameter (Table 3). The coefficient of variation equation 14; where s is the standard deviation and x̄ the arithmetic mean) makes the relative dispersion of parameters in different units directly comparable. The fact that the CV value for the maximum absorbed energy E_{max} is only 0.1% confirms that the impact energy entering all configurations was kept practically identical and that the single-variable comparison setup was successfully achieved. By contrast, the pronounced CV values observed in the parameters F_{max} (13.0%), t_t (12.6%), δ_{max} (10.0%) and Ef_{inal} (9.2%) show that, even under a constant energy input, the stacking sequence leads to a significant scatter in the response parameters, and that F_{max}, which has the highest CV, is the parameter most sensitive to the stacking architecture.

$$CV = \frac{s}{\bar{x}} \times 100 \quad (14)$$

3.2. Force–Time, Force–Displacement and Energy Response

The force–time, force–displacement and absorbed energy–time curves of the eight configurations are presented together in Figure 2. All curves exhibited the typical LVI response pattern: initially a near-linear increase of the force with the establishment of the specimen-impactor contact; then discontinuities in the curve with the triggering of damage initiation within the laminate; and after the F_{max} value is reached, a gradual decrease of the force to zero during the rebound of the impactor.

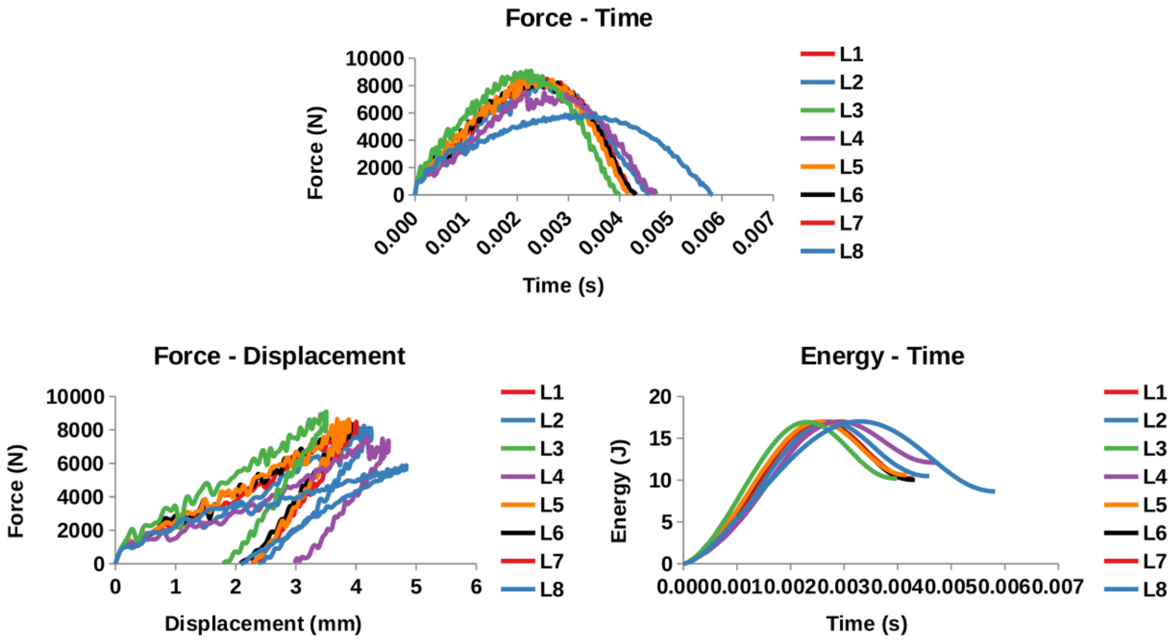

Figure 2. Impact response curves for the eight stacking configurations: Force–Time, Force–Displacement and Energy–Time.

In terms of the maximum contact force, a clear ranking emerged among the configurations. The cross-ply L3 ($[0/90]_{10s}$) exhibited the highest F_{max} value with 8964 N, while the unidirectional 90° stacking L2 exhibited the lowest F_{max} value with 5863 N. The relative difference between these two extreme values reaches 52.9%; this difference reveals the magnitude of the effect produced by the stacking architecture alone under impact load. The high value of the L3 configuration can be attributed to the high impact-bending stiffness provided by the succession of the 0° and 90° fiber directions within the 16 mm diameter contact area (Ferreira et al., 2024). The standard quasi-isotropic stacking L5 ($[0/45/-45/90]_{5s}$) ranked second in the F_{max} ranking with 8637 N; this is consistent with the design rationale for ASTM D7136 adopting the L5 stacking as the reference laminate. The F_{max} value of the blocked quasi-isotropic L8 configuration (8241 N) was about 4.6% lower than that of the dispersed L5 configuration.

3.3. Displacement and Contact Duration

The maximum impactor displacement δ_{max} is in an inverse relationship with F_{max}: L3, which has the highest F_{max} value, gave the lowest δ_{max} value (3.507 mm), while L2, which has the lowest F_{max} value, gave the highest δ_{max} value (4.836 mm). This trend is the natural consequence of the stiffness–compliance balance: a stiffer panel resists the impact with a high reaction force under a small deflection, while a softer panel dissipates the same energy with a large deflection and a low force. The relative difference in δ_{max} between L3 and L2 is 37.9%. The contact duration t_t, in the simplified mass-spring analogy, follows a square-root relationship inversely proportional to the effective stiffness of the panel (Olsson, 2000): the shortest t_t (3.93 ms) was obtained for the stiffest panel L3, and the longest t_t (5.76 ms) for the softest panel L2.

3.4. Energy Absorption

In terms of Ef_{inal}, a clear ranking emerged among the configurations. The angle-ply L4 ($[+45/-45]_{10s}$) exhibited the highest permanent absorbed energy with 12.081 J, while the unidirectional 90° stacking L2 exhibited the lowest value with 8.643 J. The relative difference between the two extremes reaches 39.8%. The high energy absorption capability of the L4 configuration arises from the ±45° fiber directions activating the matrix tension and shear damage mechanisms over a widespread area, and this behaviour has been reported similarly in the literature (Han et al., 2024; Li et al., 2024). The standard quasi-isotropic L5 stacking gave the second highest value after L4 with 10.594 J; the blocked L8 stacking exhibited an Ef_{inal} close to that of the dispersed L5 with 10.479 J (Δ = 0.115 J). This indicates that the effect of the ply-blocking on the maximum force is more pronounced than its effect on energy absorption.

3.5. Stress Distribution and Damage Mechanisms

The normal stress (S) distributions at the instant of maximum impact are presented in Figure 3. The stress concentration reached the highest values on the rear face of the impact region; since the tensile stresses in the fiber direction in this region remained below the fiber tensile strength X_t = 1500 MPa, no large-scale fiber breakage developed. By contrast, the transverse stress component governing the matrix damage exceeded the matrix tensile strength threshold Y_t = 40 MPa over a wide area around the impact; after the onset of progressive damage, matrix tension damage (DAMAGEMT) appeared widely in this region.

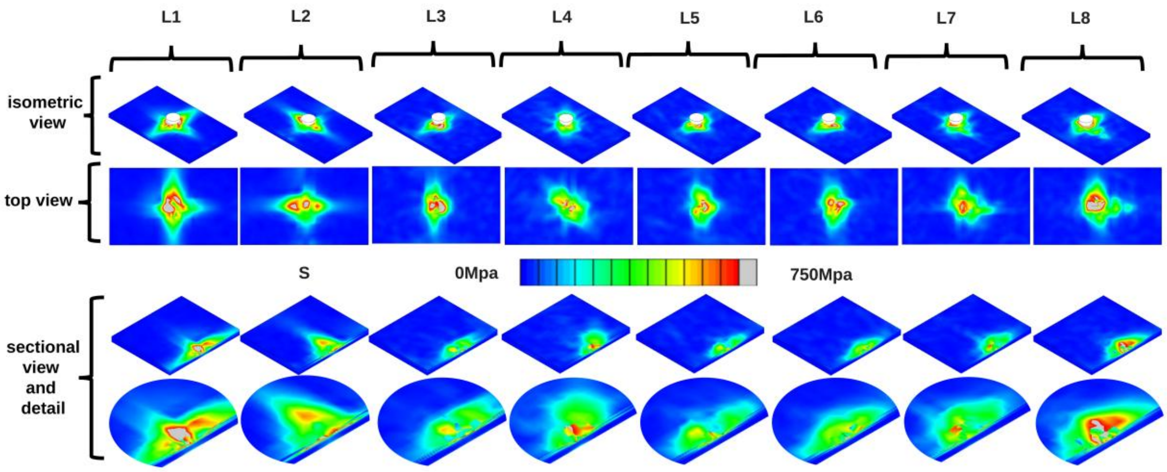

Figure 3. Normal stress (S) distributions at the instant of maximum impact (0–750 MPa): isometric, top and sectional views.

Among the four intralaminar damage variables tracked as Abaqus/Explicit output (DAMAGEFT, DAMAGEFC, DAMAGEMT, DAMAGEMC), the dominant indicator in all eight configurations emerged as matrix tension damage (DAMAGEMT). This result should be read as a model inference rather than a material finding: in this setup, in which delamination is not explicitly modelled, since the entire absorbed energy is loaded onto the intralaminar mechanisms, the emergence of the dominant indicator as DAMAGEMT is partly a result of this modelling choice. In the DAMAGEMC contours in Figure 4 and the DAMAGEMT contours in Figure 5, the geometric spread of the damage region exhibits a strong dependence on the stacking architecture.

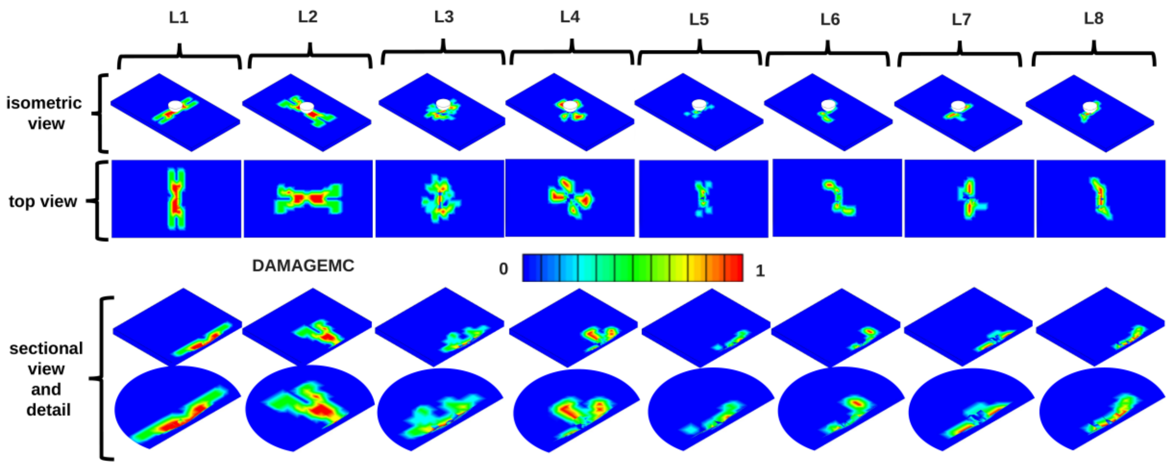

Figure 4. Matrix compression damage (DAMAGEMC) contours (scalar value 0–1): isometric, sectional and detail views.

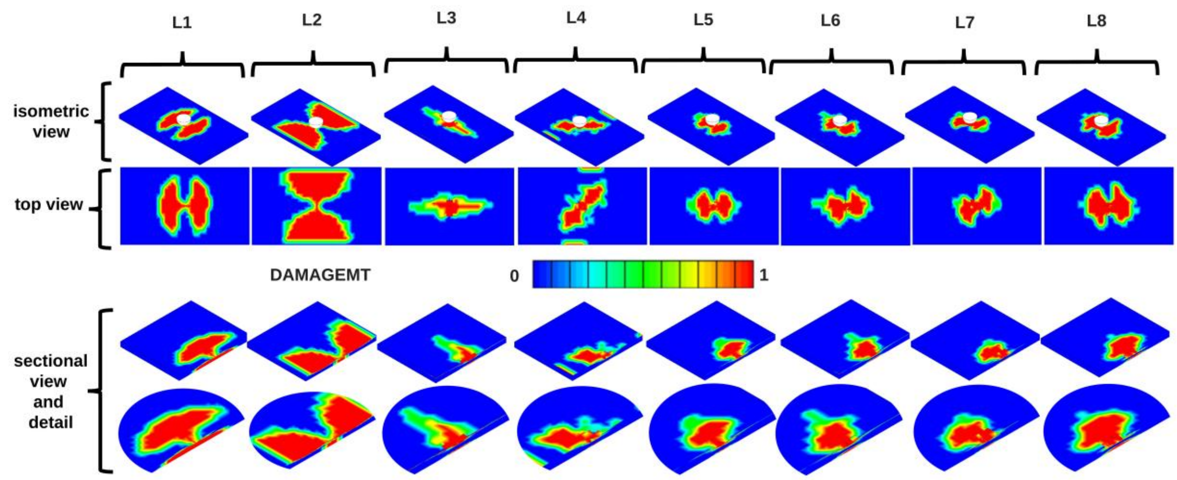

Figure 5. Matrix tension damage (DAMAGEMT) contours (scalar value 0–1): isometric, sectional and detail views.

In the unidirectional L1 and L2 stackings the damage spreads in the form of a narrow and long band along the fiber direction; in the cross-ply L3 stacking a pattern with two perpendicular arms in the 0° and 90° directions forms; and in the angle-ply L4 stacking a cross-shaped pattern following the ±45° directions appears. In the quasi-isotropic L5, multidirectional L6 and hybrid L7 configurations the DAMAGEMT contour exhibited a more circular/elliptical symmetry; in the blocked L8, on the other hand, the damage region showed a wider spread compared with the dispersed L5 (Guo et al., 2022). The damage variables in the fiber direction (DAMAGEFT, DAMAGEFC) were activated in all configurations in a narrow neighbourhood of the impact point and with limited severity; it was observed that the large-scale fiber breakage regime was not reached at the nominal 16.75 J energy level.

3.6. Performance Ranking and Critical Findings

The body of the findings shows that the effect of the stacking architecture on the LVI response has a multi-variable and partly conflicting structure. While the ranking in terms of maximum contact force (F_{max}) is L3 > L5 ≈ L7 > L6 > L8 > L4 > L1 > L2, the ranking in terms of permanent energy absorption is obtained as L4 > L5 > L8 ≈ L7 > L3 > L6 > L1 > L2. The divergence between the two rankings that becomes pronounced at the L3 and L4 extremes is the fundamental result that compels the designer to select different stackings depending on the application. The standard quasi-isotropic L5, ranking in the upper tier in both rankings, provides a balanced compromise between high contact force and good energy absorption. The comparison of the dispersed (L5) and blocked (L8) quasi-isotropic gives that ply-blocking lowers F_{max} by 4.6%, increases δ_{max} by 9.4% and decreases E_{final} by 1.1%; the consistent direction of these three parameters reveals that ply-blocking is a design decision that adversely affects the impact resistance.

3.7. Dimensionless Indicators and the Stiffness–Energy Trade-off

In order to be able to compare the response parameters of the configurations, which are in different units, within a single framework, three dimensionless/derived indicators were calculated from the primary results in Table 3 and presented in Table 4. The effective contact stiffness K*, the permanent energy absorption ratio η and the returned (elastic) energy E_r are defined by equations 15-17, respectively. These indicators reveal, independently of the absolute magnitudes, by which mechanism each stacking accommodates the impact energy.

$$K^* = \frac{F_{\max}}{\delta_{\max}} \tag{15}$$

$$\eta = \frac{E_{\text{final}}}{E_{\max}} \tag{16}$$

$$E_r = E_{\max} - E_{\text{final}}, \qquad \frac{E_r}{E_{\max}} \tag{17}$$

Table 4 makes the trade-off between stiffness and energy absorption quantitatively visible (Figure 6). The cross-ply L3 (K* = 2556 N/mm), which has the highest effective stiffness, returns about 40% of the impact energy elastically to the impactor (E_r/E_{max} = 39.9%) and its permanent absorption ratio remains at a moderate level (η = 0.601). By contrast, the angle-ply L4, with the lowest returned energy ratio (28.9%) and the highest permanent absorption ratio (η = 0.711), absorbs most of the energy through permanent damage mechanisms. This contrast positions L3 as “damage-resistant” (stiff, reflecting the energy back) and L4 as “damage-tolerant” (compliant, absorbing energy), the two extremes of structural behaviour. The unidirectional L2 stacking, with the lowest stiffness (K* = 1212 N/mm) and the highest returned energy ratio (49.2%), emerges as the weakest configuration in both performance metrics. The quasi-isotropic L5 and the multidirectional L6–L7 stackings, positioned at intermediate values in all three indicators, offer a balanced design window. This dimensionless framework shows that the stacking sequence determines not only the response magnitudes but also the distribution of the impact energy between elastic return and permanent absorption.

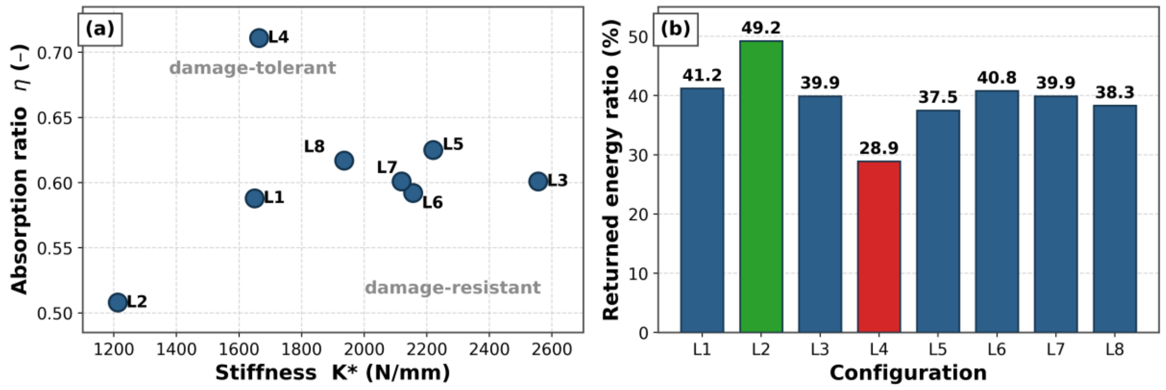

Figure 6. Assessment based on dimensionless indicators: (a) stiffness–energy trade-off map (effective stiffness K* and permanent energy absorption ratio η), (b) returned elastic energy ratio by configuration.

Table 4. Dimensionless/derived impact indicators obtained from the primary results

Config.	$K^* = F_{max}/\delta_{max}$ (N/mm)	$\eta = Ef_{inal}/E_{max}$ (–)	$E_r = E_{max} - Ef_{inal}$ (J)	E_r/E_{max} (%)
L1	1650	0.588	7.00	41.2
L2	1212	0.508	8.37	49.2
L3	2556	0.601	6.76	39.9
L4	1664	0.711	4.91	28.9
L5	2220	0.625	6.37	37.5
L6	2156	0.592	6.93	40.8
L7	2119	0.601	6.77	39.9
L8	1936	0.617	6.50	38.3

4. Discussion

4.1. The Two Conflicting Roles of the Stacking Architecture

The findings show that the effect of the stacking architecture on the LVI response is not one-dimensional, and that it gives rise to a trade-off that the structural designer is compelled to choose within. The L3 cross-ply, the leading configuration in terms of maximum contact force, has one of the lowest permanent energy absorption capabilities; by contrast, the L4 angle-ply, which exhibits the highest Ef_{inal} value, ranks in the lower tier of the F_{max} ranking. It is clear that a high F_{max} is not a desirable property in every application: a high peak force means an increase in the dynamic load transferred from the panel to the support structure and the joint elements; in ballistic protection and crash-absorber applications, the design objectives of energy dissipation and load reduction come to the fore. This behaviour exhibits a strong parallel with the trend reported by Ferreira et al. (2024) on semicylindrical woven composite shells; in the mentioned study it was revealed that the increase in the impact-bending stiffness raises the maximum force while lowering the displacement, the contact duration and the dissipated energy. In the present study, the F_{max} difference of 52.9%, the t_t difference of 46.6% and the δ_{max} difference of 37.9% between L3 and L2 support this trend also in the flat laminate geometry.

4.2. The Mechanical Basis of the Angle-Ply and Cross-Ply Stackings

The attainment of the highest Ef_{inal} value by the L4 ($[+45/-45]_{10s}$) stacking can be explained by the ±45° fiber directions simultaneously activating the matrix tensile stresses and the in-plane shear stresses, and thereby satisfying the Hashin matrix tension criterion (Hashin, 1980) over a wide region. Han et al. (2024) showed that, in carbon-glass mixed thermoplastic laminates, ±45°-dominant architectures exhibit higher energy dissipation together with a wider damage area; Li et al. (2024) presented a similar observation for hybrid woven carbon/aramid laminates. The fact that the cross-ply L3 exhibits the highest F_{max} value is related to the increase of the orthotropic bending stiffness of the unit cell formed by the 0° and 90° lamina pairs; this behaviour was also reported by Zhou et al. (2020) for cross-ply laminates. The fact that L3 ranks in the lower positions in energy absorption shows that the high stiffness works in favour of elastic energy storage and that a significant portion of the energy is returned to the impactor through reflection rather than permanent damage; indeed, in Table 4 the returned energy ratio was calculated as 39.9% for L3 and only 28.9% for L4. This makes L3 more suitable for “damage-resistant” structural components rather than “damage-tolerant” structures.

4.3. The Quasi-Isotropic Reference and the Ply-Blocking Effect

The rationale underlying the ASTM D7136 (ASTM International, 2012) standard recommending the quasi-isotropic architecture as the reference stacking for unidirectional prepregs is reinforced by the present findings: the L5 stacking ranks second in the F_{max} ranking and second in the Ef_{inal} ranking, and is positioned around the average values in terms of δ_{max} and t_t. That is, although L5 does not exhibit the highest value in any parameter, it offers a balanced performance in all parameters. Guo et al. (2022) reported that the post-impact residual compressive strength of quasi-isotropic laminates is distributed over a more predictable range; this additional property is a decisive factor in the adoption of the quasi-isotropic architecture as the standard laminate.

One of the original contributions of the present study is the direct and controlled comparison of the dispersed quasi-isotropic L5 ($[0/45/\text{-}45/90]_{5s}$) and blocked quasi-isotropic L8 ($[0_5/45_5/\text{-}45_5/90_5]_s$) stackings. The two configurations have the same total fiber-angle content, the same number of plies and the same thickness; the only difference between them is whether the fiber directions are dispersed through the thickness or grouped in blocks of five plies. The numerical results reveal that ply-blocking leads to a consistent adverse effect in three response parameters. The mechanism underlying this behaviour can be interpreted as the same-direction laminae grouped in blocks piling the stress transfer onto the inter-block interface (Guo et al., 2022). In the dispersed L5 architecture, since each lamina is surrounded by neighbours of different fiber directions, the stress transfer is distributed more homogeneously; in L8, on the other hand, since the middle laminae within a block are surrounded by same-direction laminae, the stress piles onto the inter-block interface. Similarly, Liu et al. (2022) revealed that an increase in the level of ply-blocking increases the fracture toughness in the fiber direction but spreads interlaminar separation and matrix splitting. Caminero et al. (2018), on the other hand, experimentally demonstrated the decisive role of thickness and ply-stacking sequence in impact damage tolerance and reported that angle-ply stackings behave superiorly in terms of damage tolerance. Patel (2025), in turn, reported that the dominant damage in CFRP laminates is matrix tension and interlaminar separation, and that the quasi-isotropic stacking exhibits the highest impact resistance.

4.4. Limitations of the Study

There are important limitations that should be taken into account when interpreting the findings of the present study. The absence of direct experimental validation is the most important limitation; the findings are therefore meaningful at a relative (comparative) level and do not claim quantitative precision for the absolute magnitudes. Secondly, interlaminar separation (delamination) was not included in the model in accordance with the intralaminar-only model. The mixed-mode cohesive zone approach developed by Camanho et al. (2003) has become standard in modern LVI simulations (Ferreira et al., 2023b); the exclusion of delamination causes the entire absorbed energy to be distributed among the intralaminar mechanisms and means that the emergence of DAMAGEMT as the dominant indicator is partly a result of this modelling decision. Since it has been reported that in real experiments delamination constitutes a significant portion of the total absorbed energy (Rezasefat et al., 2023), the present F_{max} and Ef_{inal} values most probably remain slightly above the experimental reference values. In the literature, it has been shown that as the impact energy increases the interlaminar separation area grows markedly (Yang et al., 2024), and it has also been reported that matrix cracks directly trigger the onset of interlaminar separation (Tan et al., 2019). For this reason, the exclusion of the cohesive interface model (Camanho et al., 2003) causes the entire absorbed energy to be loaded onto the intralaminar mechanisms and may lead the obtained F_{max} and Ef_{inal} values to remain somewhat higher compared with the experimental references.

The symmetric assumption in which the tensile and compressive strengths in the fiber direction are taken to be equal (X_t = Xc = 1500 MPa) is another limitation. In reality, in carbon/epoxy prepreg systems such as T300/5208, fiber compressive damage is triggered by different micro-mechanisms such as fiber kinking and micro-buckling, and the compressive strength is significantly lower than the tensile strength. This assumption may underpredict the fiber compressive damage (DAMAGEFC), particularly in regions where localized bending is severe under the impactor. Nevertheless, since at the present 16.75 J energy level the stresses in the fiber direction remain below the fiber strength, the effect of this assumption on the global response is considered to be limited.

The choice of the impact energy also constitutes a limitation. The present study addressed only the 16.75 J controlled energy level; since at the standard 33.5 J or higher energies fiber breakage and large-scale delamination would come into play (Rezasefat et al., 2023; Shang et al., 2025), the stacking rankings may change. Indeed, Yang et al. (2024) showed that with increasing impact energy in the 5–25 J range, both the interlaminar separation area and the intralaminar tension damage grow. Accordingly, the high contact-force superiority observed for the cross-ply L3 at the 33.5 J level may diminish as fiber breakage becomes dominant, and the divergence between the stiffness-based ranking and the energy-absorption-based ranking may become even more pronounced. In addition, repeated impact scenarios and compression after impact (CAI) tests were left out of scope; Mutsuddy et al. (2025) and Zhao et al. (2024) emphasized that repeated impact and CAI evaluation are critical in terms of damage tolerance. Despite the explicit declaration of these limitations, the present study offers a consistent reference framework enabling the direct comparison of eight stacking configurations within the same numerical scope.

5. Conclusion

In this study, the low-velocity impact response of eight stacking configurations (L1–L8), 5 mm thick and 125 × 75 mm in size, based on the T300/5208 prepreg system, was modelled in the Abaqus/Explicit environment with

SC8R continuum shell elements and within the intralaminar-only model (Hashin-CDM) framework. The main findings obtained are summarized below:

(1) Under the controlled 16.75 J impact energy, the stacking architecture leads to a difference of about 53% in maximum contact force, 38% in maximum displacement, 46.6% in contact duration and 40% in permanent absorbed energy.

(2) The cross-ply L3 exhibited the highest peak contact force and effective stiffness; it is a candidate configuration for objectives of high stiffness and low deflection such as structural panel applications.

(3) The angle-ply L4 exhibited the highest permanent energy absorption value (12.081 J); the activation of the matrix tension/shear damage over a wide area by the ±45° fiber directions is the fundamental mechanism of this behaviour.

(4) The standard quasi-isotropic stacking L5, although it does not give the highest value in any parameter, offers a balanced performance in all parameters; this balance is consistent with the ASTM D7136 standard adopting this stacking as the reference laminate.

(5) Within the present intralaminar-only model framework, the dominant damage indicator emerged as matrix tension damage (DAMAGEMT).

(6) Ply-blocking (L8), by lowering the maximum force and increasing the displacement compared with the dispersed quasi-isotropic (L5), constituted a design disadvantage within the examined scope.

(7) The dimensionless indicators derived from the primary results (effective stiffness K*, permanent absorption ratio η and returned energy ratio) quantitatively demonstrated the trade-off between stiffness and energy absorption; in this framework L3 represents "damage-resistant" behaviour with high stiffness and 39.9% elastic return, while L4 represents "damage-tolerant" behaviour with high permanent absorption (η = 0.711).

The directions recommended as a priority in future studies are as follows: calibration of the numerical model through drop-weight impact tests compliant with the ASTM D7136 protocol for at least the L3, L4, L5 and L8 stackings; integration of delamination damage into the model on the basis of the mixed-mode cohesive zone formulation; evaluation of the energy sensitivity of the stacking rankings through a parametric investigation at least at the 10 J, 16.75 J and 33.5 J energy levels; and the separation of the "damage-resistant" and "damage-tolerant" rankings through compression after impact (CAI) residual strength measurements.

Author Contribution Statement

The percentages of the author' contributions are presented below. The author reviewed and approved the final version of the manuscript.

	O.G.
C	100
D	100
S	100
DCP	100
DAI	100
LS	100
W	100
CR	100
SR	100
PM	100
FA	100

C = concept, D = design, S = supervision, DCP = data collection and/or processing, DAI = data analysis and/or interpretation, LS = literature search, W = writing, CR = critical review, SR = submission and revision, PM = project management, FA = funding acquisition.

Conflict of Interest Statement

The author declares that there is no conflict of interest in this study.

Ethical Approval Statement

Since no study was conducted on animals or humans in this research, ethics committee approval was not obtained.

References

Abrate, S. (1991). Impact on laminated composite materials. *Applied Mechanics Reviews*, *44*(4), 155–190. https://doi.org/10.1115/1.3119500

Abrate, S. (1998). *Impact on composite structures*. Cambridge University Press.

Ait Mohammed, M., & Tarfaoui, M. (2022). A progressive damage modelling of glass/epoxy cylindrical structure subjected to low-velocity impact. *Engineering Failure Analysis*, *134*, Article 106036. https://doi.org/10.1016/j.engfailanal.2022.106036

Albayrak, M., Kaman, M. O., & Bozkurt, İ. (2023). The effect of lamina configuration on low-velocity impact behaviour for glassfiber/rubber curved composites. *Journal of Composite Materials*, *57*(15), 2675–2707. https://doi.org/10.1177/00219983231175864

ASTM International. (2012). *Standard test method for measuring the damage resistance of a fiber-reinforced polymer matrix composite to a drop-weight impact event* (ASTM D7136/D7136M-12). https://doi.org/10.1520/D7136_D7136M-12

Belytschko, T., Lin, J. I., & Tsay, C. S. (1984). Explicit algorithms for the nonlinear dynamics of shells. *Computer Methods in Applied Mechanics and Engineering*, *42*(2), 225–251. https://doi.org/10.1016/0045-7825(84)90026-4

Camanho, P. P., Davila, C. G., & de Moura, M. F. (2003). Numerical simulation of mixed-mode progressive delamination in composite materials. *Journal of Composite Materials*, *37*(16), 1415–1438. https://doi.org/10.1177/0021998303034505

Caminero, M. A., García-Moreno, I., & Rodríguez, G. P. (2018). Experimental study of the influence of thickness and ply-stacking sequence on the compression after impact strength of carbon fibre reinforced epoxy laminates. *Polymer Testing*, *66*, 360–370. https://doi.org/10.1016/j.polymertesting.2018.02.009

Cao, H., Ma, M., Jiang, M., Sun, L., Zhang, L., Jia, L., Tian, A., & Liang, J. (2020). Experimental investigation of impactor diameter effect on low-velocity impact response of CFRP laminates in a drop-weight impact event. *Materials*, *13*(18), Article 4131. https://doi.org/10.3390/ma13184131

Dağ, T., Güvenç, M. A., & Uyaner, M. (2024). Low velocity impact behavior of curved composite panels reinforced with different types of stiffeners used in air vehicle. *Journal of Materials and Mechatronics: A*, *5*(1), 117–129. https://doi.org/10.55546/jmm.1459415

Davies, G. A. O., & Olsson, R. (2004). Impact on composite structures. *The Aeronautical Journal*, *108*(1089), 541–563. https://doi.org/10.1017/S0001924000000385

Ferreira, L. M., Coelho, C. A. C. P., & Reis, P. N. B. (2023a). Numerical simulations of the low-velocity impact response of semicylindrical woven composite shells. *Materials*, *16*(9), Article 3442. https://doi.org/10.3390/ma16093442

Ferreira, L. M., Coelho, C. A. C. P., & Reis, P. N. B. (2023b). Effect of cohesive properties on low-velocity impact simulations of woven composite shells. *Applied Sciences*, *13*(12), Article 6948. https://doi.org/10.3390/app13126948

Ferreira, L. M., Muñoz-Reja, M., & Reis, P. N. B. (2024). Impact response of semicylindrical woven composite shells: The effect of stacking sequence. *International Journal of Impact Engineering*, *189*, Article 104952. https://doi.org/10.1016/j.ijimpeng.2024.104952

Ghelli, D., & Minak, G. (2011). Low velocity impact and compression after impact tests on thin carbon/epoxy laminates. *Composites Part B: Engineering*, *42*(7), 2067–2079. https://doi.org/10.1016/j.compositesb.2011.04.017

Gómez-del Río, T., Zaera, R., Barbero, E., & Navarro, C. (2005). Damage in CFRPs due to low velocity impact at low temperature. *Composites Part B: Engineering*, *36*(1), 41–50. https://doi.org/10.1016/j.compositesb.2004.04.003

Gök, O. (2026). Effect of curvature height on the low-velocity impact behaviour of unidirectional T300/5208 CFRP laminated shell panels: A comparative numerical parametric analysis of intralaminar + interlaminar and intralaminar-only models. *Polymers*, *18*(11), Article 1290. https://doi.org/10.3390/polym18111290

Guo, S., Li, X., Liu, T., Bu, G., & Bai, J. (2022). Parametric study on low-velocity impact (LVI) damage and compression after impact (CAI) strength of composite laminates. *Polymers*, *14*(23), Article 5200. https://doi.org/10.3390/polym14235200

Han, L., Qi, H., Yang, J., Chu, F., Lin, C., Liu, P., & Zhang, Q. (2024). Study on the low-velocity impact response and damage mechanisms of thermoplastic composites. *Polymers*, *16*(6), Article 791. https://doi.org/10.3390/polym16060791

Hashin, Z. (1980). Failure criteria for unidirectional fiber composites. *Journal of Applied Mechanics*, *47*(2), 329–334. https://doi.org/10.1115/1.3153664

Hongkarnjanakul, N., Bouvet, C., & Rivallant, S. (2013). Validation of low velocity impact modelling on different stacking sequences of CFRP laminates and influence of fibre failure. *Composite Structures*, *106*, 549–559. https://doi.org/10.1016/j.compstruct.2013.07.008

Huang, L., Tao, Y., Sun, J., Zhang, D., & Zhao, J. (2023). Assessment of numerical modeling approaches for thin composite laminates under low-velocity impact. *Thin-Walled Structures*, *191*, Article 111053. https://doi.org/10.1016/j.tws.2023.111053

Krueger, R. (2005). *Computational fracture mechanics for composites: State of the art and challenges* (NASA/TM-2005-213530). NASA Langley Research Center.

Lapczyk, I., & Hurtado, J. A. (2007). Progressive damage modeling in fiber-reinforced materials. *Composites Part A: Applied Science and Manufacturing*, *38*(11), 2333–2341. https://doi.org/10.1016/j.compositesa.2007.01.017

Li, Y., Jin, Y., Chang, X., Shang, Y., & Cai, D. (2024). On low-velocity impact response and compression after impact of hybrid woven composite laminates. *Coatings*, *14*(8), Article 986. https://doi.org/10.3390/coatings14080986

Liu, J. L., Zhi, J., Wong, H. L., Sugeng, E. S., Tay, T. E., & Tan, V. B. C. (2022). Effect of ply blocking on the high-speed impact performance of thin-ply CFRP laminates. *Composites Science and Technology*, *228*, Article 109640. https://doi.org/10.1016/j.compscitech.2022.109640

Matzenmiller, A., Lubliner, J., & Taylor, R. L. (1995). A constitutive model for anisotropic damage in fiber-composites. *Mechanics of Materials*, *20*(2), 125–152. https://doi.org/10.1016/0167-6636(94)00053-0

Mohsin, M. A. A., Iannucci, L., & Greenhalgh, E. S. (2021). Experimental and numerical analysis of low-velocity impact of carbon fibre-based non-crimp fabric reinforced thermoplastic composites. *Polymers*, *13*(21), Article 3642. https://doi.org/10.3390/polym13213642

Mutsuddy, S., Cai, D., Hossain, M. H., & Wang, X. (2025). Repeated low-velocity impact properties of hybrid woven composite laminates. *Materials*, *18*(20), Article 4774. https://doi.org/10.3390/ma18204774

Olsson, R. (2000). Mass criterion for wave controlled impact response of composite plates. *Composites Part A: Applied Science and Manufacturing*, *31*(8), 879–887. https://doi.org/10.1016/S1359-835X(00)00020-8

Patel, S. (2025). Assessment of ply stacking sequence effect on damage behavior of CFRP composite laminate under low-velocity impacts. *Advances in Materials Science and Engineering*, *2025*, Article 4349535. https://doi.org/10.1155/amse/4349535

Pinho, S. T., Robinson, P., & Iannucci, L. (2006). Fracture toughness of the tensile and compressive fibre failure modes in laminated composites. *Composites Science and Technology*, *66*(13), 2069–2079. https://doi.org/10.1016/j.compscitech.2005.12.023

Puck, A., & Schürmann, H. (2002). Failure analysis of FRP laminates by means of physically based phenomenological models. *Composites Science and Technology*, *62*(12–13), 1633–1662. https://doi.org/10.1016/S0266-3538(01)00208-1

Reddy, J. N. (2003). *Mechanics of laminated composite plates and shells: Theory and analysis* (2nd ed.). CRC Press.

Rezasefat, M., Beligni, A., Sbarufatti, C., Amico, S. C., & Manes, A. (2023). Experimental and numerical study of the influence of pre-existing impact damage on the low-velocity impact response of CFRP panels. *Materials*, *16*(3), Article 914. https://doi.org/10.3390/ma16030914

Rezasefat, M., Gonzalez-Jimenez, A., Giglio, M., & Manes, A. (2021). Numerical study on the dynamic progressive failure due to low-velocity repeated impacts in thin CFRP laminated composite plates. *Thin-Walled Structures*, *167*, Article 108220. https://doi.org/10.1016/j.tws.2021.108220

Seifoori, S., Mahdian Parrany, A., & Mirzarahmani, S. (2021). Impact damage detection in CFRP and GFRP curved composite laminates subjected to low-velocity impacts. *Composite Structures*, *261*, Article 113278. https://doi.org/10.1016/j.compstruct.2020.113278

Shang, Y., Ma, X., Feng, C., Ding, Y., & Ma, K. (2025). Study of low-velocity impact damage in composite laminates based on crack energy. *Fibers*, *13*(9), Article 115. https://doi.org/10.3390/fib13090115

Sun, M., Chang, M., Wang, Z., Li, H., & Sun, X. (2018). Experimental and simulation study of low-velocity impact on glass fiber composite laminates with reinforcing shape memory alloys at different layer positions. *Applied Sciences*, *8*(12), Article 2405. https://doi.org/10.3390/app8122405

Tan, R., Xu, J., Sun, W., Liu, Z., Guan, Z., & Guo, X. (2019). Relationship between matrix cracking and delamination in CFRP cross-ply laminates subjected to low velocity impact. *Materials*, *12*(23), Article 3990. https://doi.org/10.3390/ma12233990

Tsai, S. W., & Hahn, H. T. (1980). *Introduction to composite materials*. Technomic Publishing.

Tsai, S. W., & Wu, E. M. (1971). A general theory of strength for anisotropic materials. *Journal of Composite Materials*, *5*(1), 58–80. https://doi.org/10.1177/002199837100500106

Vlach, J., Doubrava, R., Ruzek, R., Raska, J., Hornas, J., & Kadlec, M. (2022). Strain-field modifications in the surroundings of impact damage of carbon/epoxy laminate. *Polymers*, *14*(16), Article 3243. https://doi.org/10.3390/polym14163243

Xiong, X., Wang, Z., Zhang, Z., Li, Q., Shen, C., Fan, F., Li, X., & Chen, M. (2023). Simulation and experiment on the low-velocity impact response of flax fabric reinforced composites. *Materials*, *16*(9), Article 3489. https://doi.org/10.3390/ma16093489

Yang, L., Huang, X., Liao, Z., Wei, Z., & Zou, J. (2024). Experimental and simulation study on failure of thermoplastic carbon fiber composite laminates under low-velocity impact. *Polymers*, *16*(18), Article 2581. https://doi.org/10.3390/polym16182581

Zhang, H., Wang, M., Wen, W., Xu, Y., Cui, H., & Chen, J. (2018). A full-process numerical analyzing method of low-velocity impact damage and residual strength for stitched composites. *Applied Sciences*, *8*(12), Article 2698. https://doi.org/10.3390/app8122698

Zhao, J., Guo, Z., Lyu, Q., & Wang, B. (2024). Prediction of residual compressive strength after impact based on acoustic emission characteristic parameters. *Polymers*, *16*(13), Article 1780. https://doi.org/10.3390/polym16131780

Zhou, J., Liu, B., & Wang, S. (2022). Finite element analysis on impact response and damage mechanism of composite laminates under single and repeated low-velocity impact. *Aerospace Science and Technology*, *129*, Article 107810. https://doi.org/10.1016/j.ast.2022.107810

Zhou, J., Wen, P., & Wang, S. (2020). Numerical investigation on the repeated low-velocity impact behavior of composite laminates. *Composites Part B: Engineering*, Article 107771. https://doi.org/10.1016/j.compositesb.2020.107771